

# 1 Modelling the emergence of whisker 2 barrels

3 **Sebastian S. James<sup>1\*</sup>, Leah A. Krubitzer<sup>2</sup>, Stuart P. Wilson<sup>1</sup>**

\*For correspondence:

[seb.james@sheffield.ac.uk](mailto:seb.james@sheffield.ac.uk) (SSJ)

4 <sup>1</sup>Department of Psychology, The University of Sheffield, Sheffield, United Kingdom.;

5 <sup>2</sup>Center for Neuroscience, The University of California, Davis, United States.

6

---

7 **Abstract** Brain development relies on an interplay between genetic specification and  
8 self-organization. Striking examples of this relationship can be found in the somatosensory  
9 brainstem, thalamus, and cortex of rats and mice, where the arrangement of the facial whiskers  
10 is preserved in the arrangement of cell aggregates to form precise somatotopic maps. We show  
11 in simulation how realistic whisker maps can self-organize, by assuming that information is  
12 exchanged between adjacent cells only, under the guidance of gene expression gradients. The  
13 resulting model provides a simple account of how patterns of gene expression can constrain  
14 spontaneous pattern formation to faithfully reproduce functional maps in subsequent brain  
15 structures.

16

---

## 17 Introduction

18 Spatial patterns in neural connectivity provide clues about the constraints under which brains  
19 evolve and develop (*Purves et al., 1992*). Perhaps the most distinctive pattern can be found in the  
20 barrel cortex of many rodent species (*Woolsey and Van der Loos, 1970*). The barrels are identifiable  
21 soon after birth in layer 4 of primary somatosensory cortex as dense clusters of thalamocortical  
22 axons, which are enclosed by borders a few neurons thick from postnatal day 3 (*Erzurumlu and*  
23 *Gaspar, 2012*). In the plane tangential to the cortical surface the barrels constitute a somatotopic  
24 map of the whiskers, with cells within adjacent barrels responding most strongly and quickly to de-  
25 flection of adjacent whiskers (*Armstrong-James et al., 1992*). Barrel patterning reflects subcortical  
26 whisker maps comprising cell aggregates called barrelettes in the brainstem and barreloids in the  
27 thalamus (*Ma, 1991; Van Der Loos, 1976*).

28 Barrel formation requires afferent input from whisker stimulation and thalamic calcium waves  
29 (*Antón-Bolaños et al., 2019*), and depends on a complex network of axon guidance molecules such  
30 as ephrin-A5 and A7 and adhesion molecules such as cadherin-6 and 8 (*Vanderhaeghen et al., 2000*;  
31 *Miller et al., 2006*). This network is orchestrated by interactions between morphogens Fgf8 and  
32 Fgf17 and transcription factors Emx2, Pax6, Sp8, and Coup-tf1 (*Shimogori and Grove, 2005; Bishop*  
33 *et al., 2000*), which are expressed in gradients spanning the cortical sheet that mark orthogonal  
34 axes and can be manipulated to stretch, shrink, shift, and even duplicate barrels (*Assimacopoulos*  
35 *et al., 2012*).

36 The barrel boundaries form a Voronoi tessellation (*Senft and Woolsey, 1991*) (Fig. 1A), suggesting  
37 that barreloid topology is preserved in the projection of thalamocortical axons into the cortex,  
38 and that a barrel forms by lateral axon branching from an initial center-point that ceases upon  
39 contact with axons branching from adjacent centers. However, the assumption of pre-arranged  
40 center-points is difficult to resolve with the observation that axons arrive in the cortical plate as  
41 an undifferentiated bundle, prior to barreloid formation (*Agmon et al., 1993*). In mice, axons from  
42 the trigeminal ganglion arrive in the principal division of the trigeminal nucleus (PrV) at E12, then

43 axons from the PrV arrive in the ventroposteromedial nucleus of the thalamus (VPM) at E17, then  
 44 axons from the VPM arrive in the cortical plate at E18/P0. Distinct whisker-related clusters then  
 45 become apparent in the PrV at P0-P1, in the VPM at P2-P3, and in the cortex at P3-P5 (*Erzurumlu*  
 46 *and Gaspar, 2012; Sehara and Kawasaki, 2011*).

47 Alternatively, reaction-diffusion dynamics could generate a Voronoi tessellation without pre-  
 48 arranged centers, by amplifying characteristic modes in a noisy initial distribution of axon branches,  
 49 as a net effect of short-range cooperative and longer-range competitive interactions. Accordingly,  
 50 the barrel pattern would be determined by the relative strength of these interactions and by the  
 51 shape of the cortical field boundary. However, intrinsic cortical dynamics alone cannot account for  
 52 the topographic correspondence between thalamic and cortical domains, the irregular sizes and  
 53 specific arrangement of the barrels in rows and arcs, or the influence of gene expression gradients.

54 The center-point and reaction-diffusion models are not mutually exclusive. Pre-organized cen-  
 55 ters could bias reaction-diffusion processes to generate specific arrangements more reliably, and  
 56 mechanisms of lateral axon branching may constitute the tension between cooperation and com-  
 57 petition required for self-organization. However, proof that barrel patterning can emerge from an  
 58 undifferentiated bundle of axons, based only on local interactions, would show that a separate  
 59 stage and/or extrinsic mechanism for pre-organizing thalamocortical connections need not be as-  
 60 sumed. To this end, we ask whether barrel maps can emerge in a system with reaction-diffusion  
 61 dynamics, under the guidance of signalling gradients, and in the absence of pre-defined centers.

## 62 Models

63 *Karbowski and Ermentrout (2004)* developed a reaction-diffusion style model of how extrinsic sig-  
 64 nalling gradients can constrain the emergence of distinct fields from intrinsic cortical dynamics.  
 65 Their model defines how the fraction of occupied synapses  $c_i(x, t)$  and the density of axon branches  
 66  $a_i(x, t)$  interact at time  $t$ , along a 1D anterior-posterior axis  $x$ , for  $N$  thalamocortical projections in-  
 67 dexed by  $i$ . The model was derived from the assumption that the rates at which  $a_i$  and  $c_i$  grow  
 68 are reciprocally coupled. Extending the original 1D model to simulate arealisation on a 2D cortical  
 69 sheet, we use  $a_i(\mathbf{x}, t)$  and  $c_i(\mathbf{x}, t)$ , and model synaptogenesis as

$$\frac{\partial c_i}{\partial t} = -\alpha c_i + \beta \left( 1 - \sum_{j=1}^N c_j \right) [a_i]^k. \quad (1)$$

70 Accordingly, where the total fraction of synaptic connections sums to one, connections decay at  
 71 rate  $\alpha$ . Otherwise,  $c_i(\mathbf{x}, t)$  increases non-linearly ( $k > 1$ ) with the density of axon branching. Axon  
 72 branching is modelled as

$$\frac{\partial a_i}{\partial t} = \nabla \cdot \left( D \nabla a_i - a_i \sum_{j=1}^M \gamma_{i,j} \nabla \rho_j(\mathbf{x}) + \chi_i \right) - \frac{\partial c_i}{\partial t}. \quad (2)$$

73 The first term on the right describes the divergence (indicated by  $\nabla \cdot$ ) of the quantity in parentheses,  
 74 which is referred to as the ‘flux’ of axonal branching. The flux represents diffusion across the  
 75 cortical sheet, at rate  $D$ , and the influence of  $M$  molecular signalling fields,  $\rho(\mathbf{x})$ . The influence of a  
 76 given field (indexed by  $j$ ) on a given thalamic projection (indexed by  $i$ ), is determined by  $\gamma_{i,j}$ , which  
 77 may be positive or negative in order that axons may branch in the direction of either higher or lower  
 78 concentrations. Note that computing the divergence in simulation requires cells on the cortical  
 79 sheet to communicate with immediately adjacent cells only (see *Materials & Methods*). Here  $\chi_i = 0$   
 80 is a placeholder. The second term on the right represents the coupling between axon branching  
 81 and synaptogenesis, and an assumption that the spatial distribution of synaptic density across the  
 82 cortical sheet is broadly homogeneous. As such, the quantity  $c_i$  can be thought of as the connection  
 83 density.

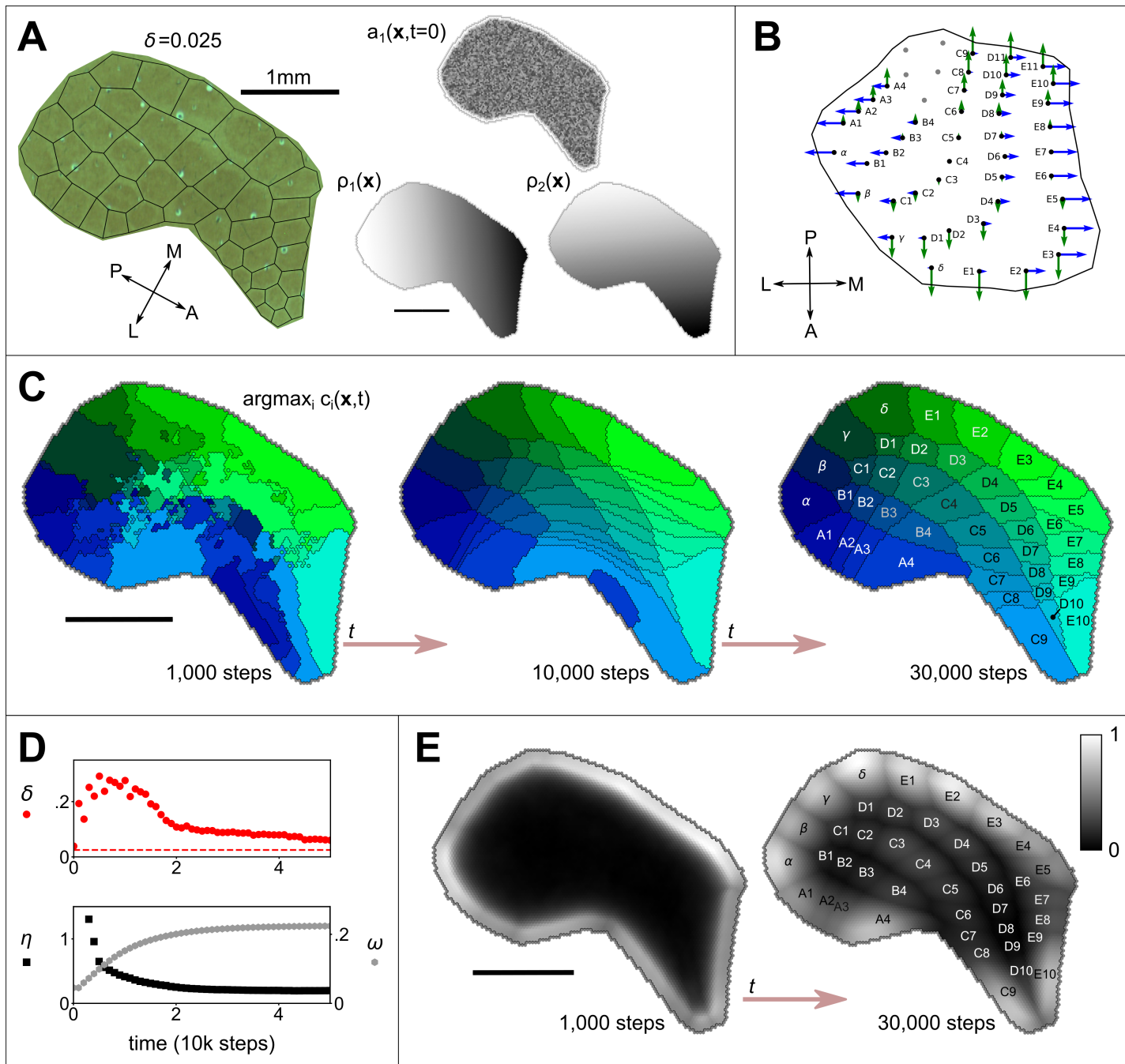


**Figure 1.** The emergence of whisker barrels. **A** Left shows a cytochrome oxidase stain obtained from rat S1 by [Zheng et al. \(2001\)](#), with black lines to delineate barrels and to measure departure (Honda- $\delta$ ; see [Senft and Woolsey, 1991](#)) from a perfect Voronoi tessellation. Right shows the initial distribution of axon branching density ( $a$ ) for one thalamocortical projection, and two molecular guidance fields ( $\rho$ , where the domain  $S$  has been traced from **A**). **B** The strengths of interaction  $\gamma$  with fields  $\rho_1$  and  $\rho_2$  are indicated for each of 41 projections by the lengths of green and blue arrows respectively, assuming that similar fields aligned to the posterior-anterior and medial-lateral axes in the ventroposterior medial nucleus of the thalamus are sampled at the locations of putative barrelloid centers (reconstructed from [Haidarliu and Ahissar, 2001](#), their Fig. 5b). **C** Results for the example simulation, with parameters  $N = 41$ ,  $\alpha = 3.6$ ,  $\beta = 16.67$ ,  $k = 3$ ,  $D = 0.5$ ,  $\gamma \in \pm 2$ ,  $\epsilon = 1.2$  and  $\delta t = 0.0001$ . Colours indicate the thalamic projection for which the connection density is maximal, barrel labels are located at the centroid of each region and black lines delineate boundaries (see Movie S1). **D** Red dots show the Honda- $\delta(t)$  metric obtained from the simulation approaching that obtained from the real barrels in **A** (dotted line); black squares show the pattern difference metric  $\eta(t)$ , and reveal the emergence of a correspondence between the real and simulated barrel shapes (units  $\text{mm}^3$ ); grey hexagons show how selectively each cortical site is innervated;  $\omega(t) = \oint_S \mu(\mathbf{x}, t) dS$ , where  $\mu(\mathbf{x}) \equiv \max_i(c_i(\mathbf{x}, t)) / \sum_{j=1}^N c_j(\mathbf{x}, t)$ . **E** Plotted across the cortical sheet, the selectivity develops to reveal an alignment with the emergent barrel boundary shapes. Greyscale colour indicates values of  $\mu(\mathbf{x})$ . All scale bars 1 mm.

84 **Results**

85 First we verified that all results established by **Karbowksi and Ermentrout (2004)** for a 1D axis could  
 86 be reproduced using our extension to a 2D cortical sheet. Using an elliptical domain,  $S$ , with  $M = 3$   
 87 offset guidance gradients aligned to the longer axis,  $N = 5$  thalamocortical projections gave rise to  
 88 five distinct cortical fields at locations that preserved the topographic ordering defined by the orig-  
 89 inal  $\gamma$  values. However, we found that specifying  $N$  ordered areas required  $M \approx (N+1)/2$  signalling  
 90 fields. This is because localization of axon densities occurs only when projections are influenced  
 91 by interactions with two or more signalling gradients that encourage migration in opposing direc-  
 92 tions. As the number of guidance fields is unlikely to approach the number of individual barrels,  
 93 modifications to the model were required.

94 We reasoned that an arbitrary number of distinct field locations may be determined by a min-  
 95 imum of two guidance gradients, if the concentration of the projection densities is influenced by  
 96 competition between projections, and if a projection that interacts more strongly with a given guid-  
 97 ance gradient migrates further in the direction of that gradient. Accordingly, projections that inter-  
 98 act most strongly with a given guidance gradient would come to occupy cortical locations at which  
 99 that field has extreme values, leaving adjacent locations available to be occupied by projections  
 100 with the next strongest interactions, and so forth. This would in principle allow the *relative* loca-  
 101 tions of the fields to be specified by the relative values of the interaction parameters,  $\gamma$ , and hence  
 102 for a topological map in the cortex to be specified by a spatial ordering of the  $\gamma$  values at the level  
 103 of the thalamus.

104 Such dynamics are quite unlike those described by classic chemospecificity models (**Sperry, 1963**),  
 105 which essentially assume center-points by specifying conditions in the target tissue that  
 106 instruct pre-identified afferents to stop growing. Consider, for example, that when simulated in  
 107 isolation from one-another, all projections in the model described would simply migrate to the  
 108 extrema of the cortical guidance fields.

109 Testing this reasoning required increasing the strength of the competition between simulated  
 110 thalamocortical projections for cortical territory, by increasing the tendency for each projection  
 111 to compete for cortical space in which to branch and make connections. The major modification  
 112 required was thus to introduce into the model an additional source of competition between thala-  
 113 mic projections. The term in parentheses in Eq. 1 represents competition between thalamocortical  
 114 projections for a limited availability of cortical connections. To introduce competition also in terms  
 115 of axon branching, whilst ensuring that  $a_i$  is conserved over time, we redefined

$$\chi_i(\mathbf{x}, t) = \frac{\epsilon a_i}{N-1} \nabla \sum_{j \neq i}^N a_j. \quad (3)$$

116 This term contributes to the *flux* of axonal branching as an additional source of diffusion, scaled  
 117 by  $\epsilon$ , which reduces the branching density for a given projection where the branches of other pro-  
 118 jections are dense. Note that this operation is local to individual afferent projections.

119 In addition, the model we have outlined requires that molecular guidance gradients in the cor-  
 120 tex are complemented by graded values of the interaction strengths,  $\gamma$ , at the level of the thalamus.  
 121 While the precise mechanisms by which thalamic and cortical gradients interact during develop-  
 122 ment have not been fully characterised, the presence of complementary thalamic and cortical guid-  
 123 ance gradients has been well established experimentally. In particular, the EphA4 receptor and its  
 124 ligand ephrin-A5 are distributed in complementary gradients in the somatosensory thalamus and  
 125 cortex (**Vanderhaeghen et al., 2000; Miller et al., 2006**).

126 Cells originating in VPM express high levels of EphA receptors and project to the lateral part  
 127 of S1, which expresses low levels of ephrin-A5, and cells originating in the VPL express low levels  
 128 of EphA receptors and project to the medial part of S1, which expresses high levels of ephrin-A5  
 129 (see **Gao et al., 1998; Dufour et al., 2003; Vanderhaeghen and Polleux, 2004; Speer and Chapman,**  
 130 **2005; Torii et al., 2013**). We assume that such patterning arises because the relative strengths of  
 131 interaction with guidance molecules (e.g., ephrin-A5) in the cortex are correlated with the relative

132 concentrations of complementary molecules (e.g., EphA4) in the thalamus, and thus with thalamic  
 133 position along the axis to which their gradients are aligned.

134 For simplicity, the two simulated thalamic interaction gradients, as well as the two cortical guid-  
 135 ance gradients, were initially chosen to be linear and orthogonal. Hence a given pair of  $\gamma$  values  
 136 corresponds to the coordinate of a barrelloid center in the VPM. Coordinates, in a reference plane  
 137 defined by the anterior-posterior and medial-lateral axes, were estimated from Fig 5d of **Haidar-**  
 138 **liu and Ahissar (2001)**, and scaled such that  $\gamma \in \pm 2$ . Note that this scaling is arbitrary because  
 139 according to the model the coordinates provide relative position information only.

140 A cortical boundary enclosing barrels for 41 macrovibrissae was traced from a cytochrome oxi-  
 141 dase stain from **Zheng et al. (2001)** (using original data kindly supplied by the authors), and Eqs. 1–3  
 142 were solved for  $N = 41$  projections on the resulting domain,  $S$ , using  $M = 2$  linear signalling gradi-  
 143 ents aligned with the anterior-posterior and medial-lateral axes. These gradients are shown with  
 144 the barrel field boundary in Fig. 1A for clarity, though like ephrin-5 they may be thought of as ex-  
 145 tending across the cortical hemisphere (**Miller et al., 2006**). Simulations were stepped through  
 146 30000 iterations of Eqs. 1–3 ( $\delta t = 0.0001$ ).

147 Across a wide range of parameter values, random initial conditions (a uniform random distri-  
 148 bution for  $a(\mathbf{x}, 0) \in (0.2, 0.4)$ ,  $c(\mathbf{x}, 0) = 0$ ) eventually yielded a clear Voronoi-like tessellation of topo-  
 149 graphically organized thalamocortical projections, confirming that barrel maps can self-organize in  
 150 the absence of pre-specified center points. The organization is apparent in a plot of the identity of  
 151 the projection for which the connection density is maximal at each simulated cortical location, as  
 152 shown in Fig. 1C. Parameter values for this example simulation (see also Movie S1) were obtained  
 153 by conducting a full parameter sweep and choosing a combination ( $\alpha = 3.6$ ,  $\beta = 16.67$ ,  $k = 3$ ,  $D = 0.5$ ,  
 154  $\epsilon = 1.2$ ) that scored well against the following three measures.

155 First, we used an algorithm introduced by Honda to measure the discrepancy of each barrel  
 156 shape from a Dirichletform shape (**Honda, 1983**). Low overall values of this *Honda*- $\delta$  metric ob-  
 157 tained from simulated barrels indicate a close correspondence of the simulated barrel field with a  
 158 Voronoi tessellation, and thus with a biological barrel field (for mice  $\delta \approx 0.054$ , **Senft and Woolsey,**  
 159 **1991**, and our analysis of data from **Zheng et al., 2001** indicates that the value for rats is similar).  
 160 For the tessellation that is overlaid on the real barrel field in Fig. 1A,  $\delta = 0.025$ , and a reduction in  $\delta$  in  
 161 the example simulation over time confirmed that an equivalent ‘good’ Voronoi pattern can emerge  
 162 within  $\approx 20000$  iterations (Fig. 1D, red circles). Second, we devised a *pattern difference* measure that  
 163 is sensitive to deviations in the component shapes and overall topographic registration between  
 164 two tessellations,  $\eta$ , and we used this measure to compare the simulated barrel fields to the real  
 165 barrel field from which the boundary shape applied to the simulation was obtained (see *Materials*  
 166 & *Methods* for details). A similar reduction in  $\eta$  in the development of the example simulation con-  
 167 firmed that the shapes and arrangement of emergent connection fields came to match those of  
 168 the real barrel field by around 20000 iterations (Fig. 1D, black squares). Third, we measured the  
 169 *connection selectivity* at each location on the cortical sheet, as the connection density of the most  
 170 dense projection divided by the sum over all projection densities,  $\omega$ . The overall connection selec-  
 171 tivity increased as the barrel map self-organized in the example simulation (Fig. 1D, grey hexagons),  
 172 and the selectivity became concentrated in regions overlapping with the emergent barrel centers  
 173 (Fig. 1E).

174 Against these three metrics we are also able to characterise the robustness of self-organization  
 175 to the model parameters, and to investigate the sensitivity of the model to variation in its inputs.  
 176 Fig. 2A shows values of  $\delta$ ,  $\eta$  and  $\omega$  obtained after 30000 iterations, from 216 independent simula-  
 177 tions, each representing a unique combination of the model parameters  $D$ ,  $\epsilon$ , and the ratio  $\alpha/\beta$ . First  
 178 we observe that self-organization is highly robust to the ratio  $\alpha/\beta$ , across five orders of magnitude,  
 179 with respect to all three metrics. Second, the most strongly Dirichletform patterns (low *Honda*- $\delta$ )  
 180 were generated by simulations in which the diffusion constant  $D$  and the strength of competition  
 181  $\epsilon$  were high. Third, strongest overall connection selectivities,  $\omega$ , were obtained for lower values  
 182 of  $D$ . Fourth, variation in the pattern difference metric,  $\eta$ , indicated that the alignment between

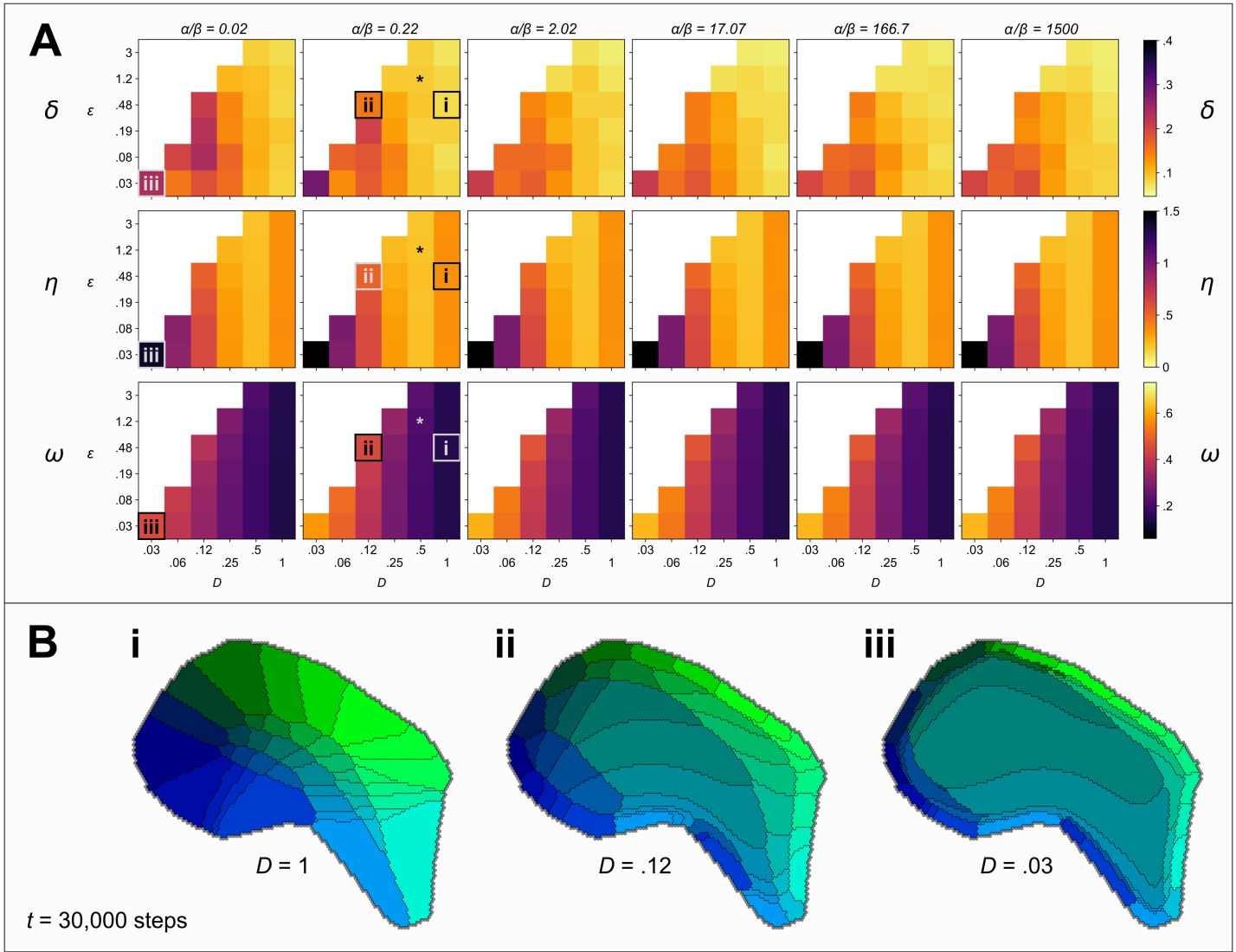


**Figure 2.** Exploring the parameter space. **A** Colour indicates the quality of the pattern at  $t = 30000$  steps, against three measures: Low values of *Honda*- $\delta$  (top row) suggest a Voronoi-like pattern of fields. The *pattern difference*,  $\eta$  (middle row) measures the difference in the area and arrangement of barrels in real and simulated fields. The *selectivity*,  $\omega$  (bottom row), measures the specificity with which the cortical sheet is innervated. Colour maps are chosen so that lighter (orange and yellow) colours indicate higher quality patterns against each measure. White squares indicate combinations of parameters for which simulations were numerically unstable. The parameter space explored is three dimensional with the ratio  $\alpha/\beta$  varying between plots, and the competition parameter  $\epsilon$  and the diffusion constant  $D$  varying within plots. An asterisk (\*) marks the parameters used in Fig. 1. Boxes i), ii) and iii) mark parameter sets for which corresponding patterns are shown in **B** (for  $t = 30000$  steps). **B** Varying the diffusion constant  $D$  generates qualitatively different patterns. Higher values cause expansions of the peripheral barrels and a corresponding compression of the inner barrels (i). Lower values instead cause an expansion of the central barrels and compression of the peripheral barrels (ii). Further reducing the rate of diffusion (iii), which is equivalent to increasing the size of the domain and hence simulating development in an animal with a larger cortex, causes a large area to be occupied by projections with intermediate interaction parameters; those with strong interaction parameters are compressed around the edge of the domain, and consequently a barrel pattern fails to form.

real and simulated patterns was greatest for intermediate rates of diffusion,  $D \approx 0.5$ . Together these results indicate that when competition is strong, the rate of diffusion determines a trade-off such that fields emerge to be barrel-shaped when diffusion is fast and they emerge to be more selectively innervated when diffusion is slow.

The parameters of the example simulation are indicated in Fig. 2A using an asterisk. In Fig. 2B, we also present examples of alternative patterns that emerge for different choices of  $D$ . Decreasing the rate of diffusion may be considered equivalent to increasing the overall size of the domain,  $S$ . Hence, insights into barrel development in species with a larger representation of the vibrissae, which do not have barrel fields, may be gained by studying pattern formation when  $D$  is small. In this context, it is interesting to note that for small  $D$ , the organization is predicted to be topological but highly irregular, with a general expansion in the territory occupied by the central versus peripheral domains that would presumably manifest as an absence of identifiable barrel fields (Fig. 2B iii).

Next we conducted a sensitivity analysis to determine the extent to which the quality of the pattern (after  $t = 30000$  iterations) is affected by perturbations to i) the magnitude and offset of the noise applied to  $a_i$  at  $t = 0$ ; ii) noise applied to the interaction parameters,  $\gamma_{i,j}$ ; iii) noise (at various length scales) applied to the guidance fields; and iv) the magnitude and orientation of one cortical guidance field relative to the other (Fig. 1A).

Using the parameters of the example simulation (Fig. 1C) we established baseline mean and standard deviations from ten independent simulations with initial uniform random values for  $a(\mathbf{x}, 0) \in (0.2, 0.4)$ , to be  $\delta = 0.089 \pm 0.004$ ,  $\eta = 0.2108 \pm 0.002$ , and  $\omega = 0.2165 \pm 0.0001$ . Repeating with the variation in the initial noise doubled ( $a(\mathbf{x}, 0) \in (0.1, 0.5)$ ), or removed altogether ( $a(\mathbf{x}, 0) = 0.3$ ), generated distributions of  $\delta$ ,  $\eta$ , and  $\omega$  that were not statistically different, as established using paired two-sample t-tests. Adding noise to the interaction parameters ( $\gamma$ ) affected neither the *Honda*- $\delta$  or the *connection selectivity* measures substantially (see Fig. 3A), and an increase in the *pattern difference* reflected an increase in the occurrence of topological defects only when perturbations become so large as to cause the ordering of  $\gamma$  values from neighbouring thalamic sites to be switched (see example map Fig. 3B i). Adding noise to the cortical guidance field values,  $\rho_1(\mathbf{x})$  and  $\rho_2(\mathbf{x})$ , disrupted pattern formation only for high levels of noise applied at short length scales, which manifested as non-straight edges at the domain boundaries (Fig. 3B ii). Varying the slope of one linear gradient  $\rho_1(\mathbf{x})$  while keeping that of the other constant caused elongation of the emergent domains along the corresponding axis (Fig. 3B iii), while pattern formation was not strongly influenced by relaxing the assumption that the gradients of the two cortical guidance fields are orthogonal (Fig. 3B iv). Overall, the sensitivity analysis revealed that self-organization of barrel-like fields in the model is highly robust to a wide range of sources of perturbation.

To further investigate the interplay of genes intrinsic to the developing neocortex and extrinsic factors such as thalamocortical input, we simulated two well known experimental manipulations of barrel development. First, we simulated a seminal barrel duplication paradigm (**Shimogori and Grove, 2005; Assimacopoulos et al., 2012**) in which the growth factor Fgf8, which is normally expressed at the anterior end of the cortical subplate from around E9.5 (**Crossley and Martin, 1995**), is ectopically expressed (by electroporation) also at the posterior pole. We assume that this results in a mirror of the primary barrel cortex boundary along the rostrocaudal axis (**Assimacopoulos et al., 2012**) and a mirroring of the anterior-posterior guidance gradient  $\rho_1$  at the border between them (Fig. 4A). The result after 30000 iterations, and otherwise using the parameters of the example simulation, was two mirror-symmetrical barrel fields comprising  $2N$  barrels (Fig. 4B), consistent with the outcome of the original experiments.

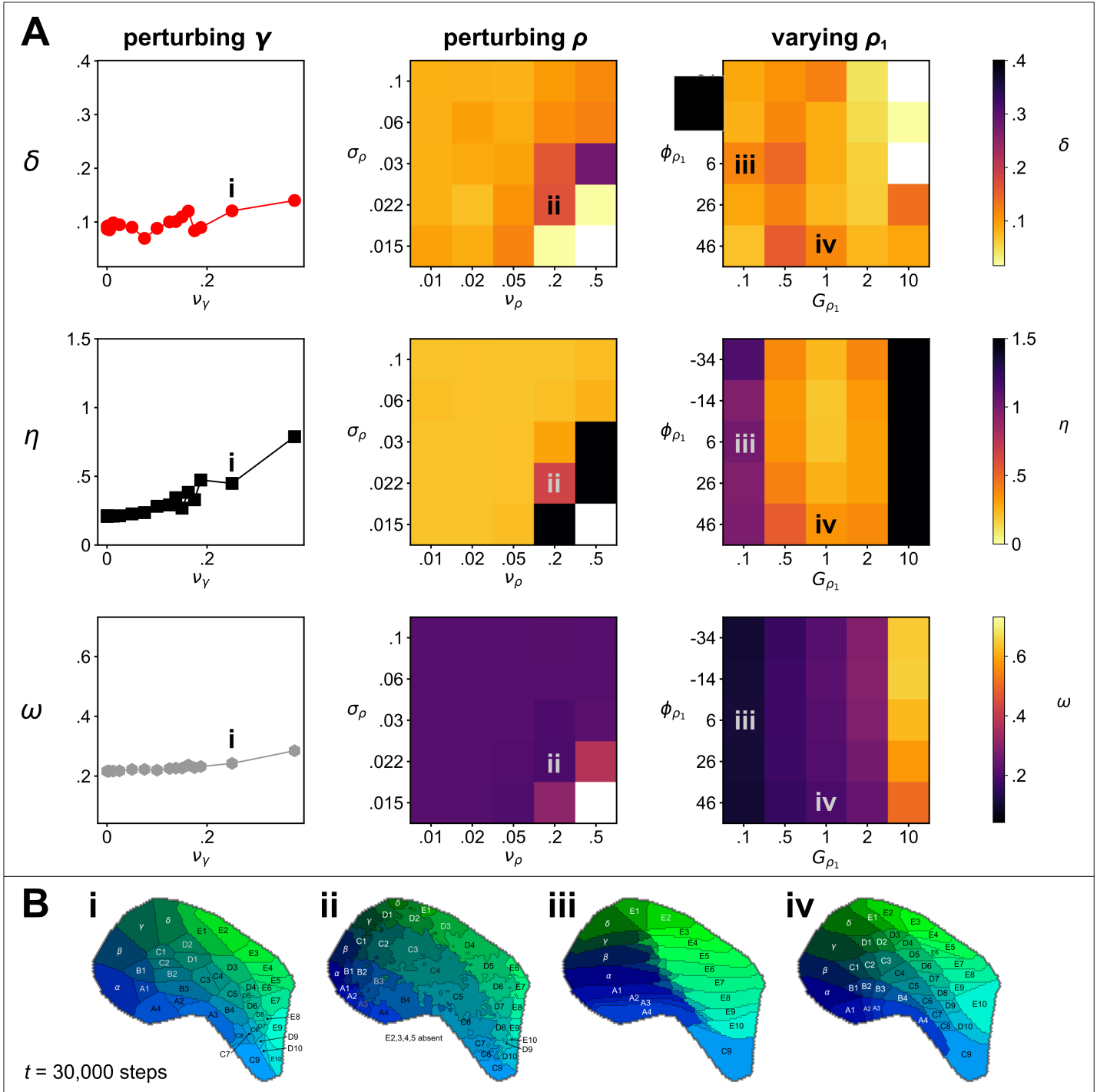


**Figure 3.** Sensitivity analysis. **A** Metrics of map quality  $\delta(t)$  (top row),  $\omega(t)$  (middle row) and  $\eta(t)$  (bottom row), were evaluated at  $t = 30000$  steps. The  $y$ -axes and colour scales have identical ranges to the colour scales in Fig. 2, for easy comparison. *Left column:* The effect of adding noise drawn from a uniform distribution,  $(\gamma_{max} - \gamma_{min}) U(0, v_\gamma)$ , to the values of the interaction parameters,  $\gamma$  used in Fig. 1. *Middle column:* The effect of changing the magnitude and the length scale of noise applied to the guidance fields. Uniform random noise  $(\rho_{max} - \rho_{min}) U(0, v_\rho)$  was added to each (hexagonal) element of  $\rho_1(\mathbf{x})$  and  $\rho_2(\mathbf{x})$  and the result was smoothed by convolution with a symmetric 2D Gaussian kernel of width  $\sigma_\rho$ . *Right column:* The effect of setting the rotational angle of the linearly varying guidance field,  $\rho_1(\mathbf{x})$ , to  $\phi_{\rho_1}$ , and modifying its overall gain to  $G_{\rho_1}$ , whilst keeping the parameters of  $\rho_2(\mathbf{x})$  unchanged from those used in the example simulation, for which  $\phi_{\rho_2} = 84^\circ$  and  $G_{\rho_2} = 1$ . **B** Four ways in which the perturbations in **A** affect the patterns. i) The effect of significant interaction parameter noise results in topological defects. ii) High magnitude, short lengthscale noise in  $\rho(\mathbf{x})$  leads to non-straight edges between adjacent barrels. iii) Reducing the slope of gradient  $\rho_1$  (by a factor of 10) causes barrel rows B, C and D to become ‘crushed’ down the center line, and edge barrels to dominate. iv) Rotating  $\rho_1$  by  $20^\circ$  causes a slight distortion of the pattern, resulting in an overall anticlockwise rotation of the field locations.

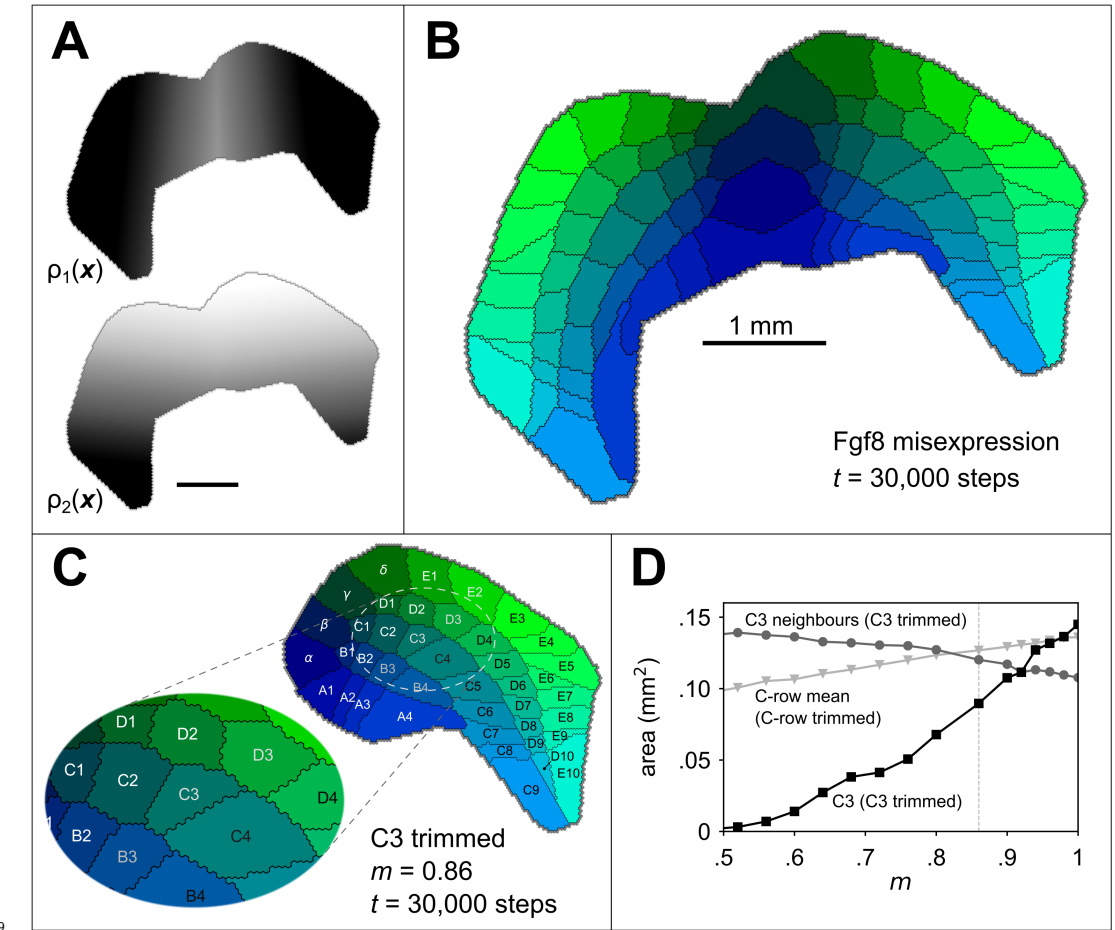


**Figure 4.** Simulating altered barrel development. Guidance fields (**A**) and emergent barrel pattern (**B**) in a Fgf8 misexpression experiment (c.f. *Assimacopoulos et al., 2012*), simulated by reflecting  $\rho_1$  from Fig. 1A at the join of the original boundary with its mirror. All other model parameters match those in Fig. 1C. **C** Simulating whisker trimming by reducing the competitiveness,  $\epsilon$ , of one projection. For C3 only,  $\epsilon$  was multiplied by  $m \in (0, 1)$ . The pattern shown is that formed after 30000 steps with  $m = 0.86$ , which reduces the size of the C3 field to 65% of its original size, matching the average barrel area reduction observed by *Kossut (1992)*. **D** The area of the C3 barrel (black squares) reduces as  $m$  is reduced, whereas the mean area of neighbouring barrels (B3, C2, C4, D2 & D3, grey circles) increases. The dotted grey line indicates  $m = 0.86$  for comparison with panel C. If the  $\epsilon$  value is instead reduced for all row C projections (including the interstitial  $\gamma$  projection), the mean row C barrel area is only slightly reduced (light grey triangles). In this case, the mean area of a simulated row C barrel at  $m = 0.86$  is 91% of that for  $m = 1$ .

Finally, to investigate the response of the model to environmental manipulation, we simulated a whisker deprivation experiment. In a critical period comprising the first postnatal days, removal of the whiskers by electrocauterization, plucking, or trimming leads to observable changes in brain structures, including the barrel field (*Jeanmonod et al., 1981*). Amongst other changes, deprivation of individual whiskers leads to smaller barrels (*Kossut, 1992*). We simulated trimming of the individual whisker C3 during the critical period by reducing the competitiveness of the C3 thalamocortical projection,  $\epsilon$ . As a result, the corresponding field size was smaller (Fig. 4C), and the size of the fields representing the neighbours of C3 increased in size. A reduction in area to 65%, comparable to that induced by *Kossut (1992)*, was obtained in simulation when  $\epsilon$  was reduced to 86% (Fig. 4D), and the C3 barrel disappeared altogether when  $\epsilon$  was less than half of its original value.

Although individual whisker trimming reduces barrel size, if an entire row is trimmed, barrel sizes for the trimmed row are not obviously changed (*Land and Simons, 1985*). We investigated with a simulation in which we varied  $\epsilon$  for all of the row C projections. Although the barrels which formed for row C did show some reduction in area (Fig. 4D), this reduction was small when compared with

245 the individually trimmed C3 simulation. If the effect of trimming any whisker is to reduce its  $\epsilon$   
 246 (the competitiveness of its projection) to 86% of its original value, then the model predicts that the  
 247 cortical barrels for the trimmed C row will retain 91% of their area on average.

248 Together with the results of simulated misexpression, the consistency of the simulated whisker  
 249 trimming results with those of the original studies demonstrates how the model can be used to  
 250 investigate the contribution of intrinsic and extrinsic factors to the development of cortical fields.

## 251 Discussion

252 The present results suggest that the key requirements for the emergence of realistic barrel pat-  
 253 ttering are i) at each cortical location thalamocortical projections compete for a limited number  
 254 of available synaptic connections (Eqs. 1–2), ii) at each location the branching rate of a given pro-  
 255 jection is reduced by the density of other projections (Eq. 3), and iii) the branch density of each  
 256 projection is conserved over time.

257 The emergence of barrels in simulation required competition between thalamic projections in  
 258 terms of synaptic connectivity and also competition in terms of cortical space, as represented by  
 259  $\chi$ , with an implicit requirement for a self/other identifier amongst projections. This latter form of  
 260 competition may account for the absence of barrels in rodents with larger brains, such as capybara,  
 261 for which competition for space is presumably weaker (*Woolsey et al., 1975*). Hence, irrespective  
 262 of whether barrels are necessary for adaptive whisker function, the emergence of somatotopically  
 263 ordered modular structures may be an inevitable consequence of local competition for cortical  
 264 territory driven by input from an array of discrete sensory organs (*Purves et al., 1992*).

265 In reality, scores of smaller Dirichletform barrels representing the microvibrissae form along-  
 266 side the E-row barrels, presumably via the same competitive processes. Enforcing here the same  
 267 boundary condition as used to represent the true edges of the barrel field was necessary to en-  
 268 sure the stability of the simulation, though we acknowledge that this region of the boundary was  
 269 enforced primarily to keep the number of simulated projections, and hence the overall computa-  
 270 tional complexity of the simulation, manageable (simulating an extra projection introduces 13030  
 271 new dynamical variables).

272 It is important to emphasize that the formulation of the model is entirely local, insofar as simu-  
 273 lation requires no information to be communicated from a given cortical grid cell to any but those  
 274 immediately adjacent (via diffusion). Hence the simulations demonstrate how a self-organizing  
 275 system, constrained by genetically specified guidance cues and by the shape of the cortical field  
 276 boundary, can faithfully reproduce an arrangement of cell aggregates in one neural structure as a  
 277 topographic map in another.

278 Moreover, the present results confirm that somatotopic map formation does not require the  
 279 pre-specification of center-points by as yet undetermined additional developmental mechanisms.

## 280 Materials & Methods

281 We concentrated on the representation of the forty-one macrovibrissae that constitute a given  
 282 barrel field, because their thalamic and cortical correlates are easily identifiable and consistently  
 283 located, excluding the five rhinal whiskers as their cortical representation is isolated from the main  
 284 barrel field. We excluded the representation of the microvibrissae to limit the overall complexity  
 285 of the simulations.

286 The cortical sheet was modelled as a two dimensional hexagonal lattice, which simplifies the  
 287 computation of the 2D Laplacian. Within a boundary traced around the edge of a rat barrel field  
 288 (Fig. 1A) we set the hex-to-hex distance  $d$  to 0.03 mm, which resulted in a lattice containing 6515  
 289 hexes for the simulations shown in Figs. 1A,C & D and 12739 hexes for the Fgf8 misexpression  
 290 study shown in Fig. 4. Each hex contained 82 time-dependent variables: 41 branching densities  
 291 ( $a_i$ ) and 41 connection densities ( $c_i$ ). The rate of change of each of the time-dependent variables  
 292 (Eqs. 1 & 2) was computed using a fourth-order Runge-Kutta method.

293 The most involved part of this computation is to find the divergence of the flux of axonal branching-  
 294 ing,  $\mathbf{J}_i(\mathbf{x}, t)$ , the term in parentheses in Eq. 2:

$$\nabla \cdot \mathbf{J}_i(\mathbf{x}, t) = \nabla \cdot \left( D \nabla a_i - a_i \sum_{j=1}^M \gamma_{i,j} \nabla \rho_j(\mathbf{x}) + \frac{\epsilon a_i}{N-1} \nabla \hat{a}_i \right), \quad (4)$$

295 where  $\hat{a}_i \equiv \sum_{j \neq i}^N a_j$ . Note that the sum of the guidance gradients is time-independent and define  
 296  $\mathbf{g}_i(\mathbf{x}) \equiv \sum_{j=1}^M \gamma_{i,j} \nabla \rho_j(\mathbf{x})$ . Because the divergence operator is distributive, Eq. 4 can be expanded  
 297 using vector calculus identities (dropping references to  $\mathbf{x}$  and  $t$  for clarity):

$$\nabla \cdot \mathbf{J}_i = \nabla \cdot (D \nabla a_i) - \nabla \cdot (a_i \mathbf{g}_i) + \frac{\epsilon}{N-1} \nabla \cdot (a_i \nabla \hat{a}_i). \quad (5)$$

298 Applying the vector calculus product rule identity yields

$$\nabla \cdot \mathbf{J}_i = D \nabla \cdot \nabla a_i - a_i \nabla \cdot \mathbf{g}_i - \mathbf{g}_i \cdot \nabla a_i + \frac{\epsilon a_i}{N-1} \nabla \cdot \nabla \hat{a}_i + \frac{\epsilon}{N-1} \nabla \hat{a}_i \cdot \nabla a_i, \quad (6)$$

299 which has five elements to compute: i)  $D \nabla \cdot \nabla a_i$  (the Laplacian of  $a_i$ ); ii) a time-independent modula-  
 300 tor of  $a_i$  (because  $\nabla \cdot \mathbf{g}_i$  is a time-independent static field); iii) the scalar product of the static vector  
 301 field  $\mathbf{g}_i$  and the gradient of  $a_i$ ; iv) the Laplacian of  $\hat{a}_i$ ; and v) a term involving the gradients of  $a_i$  and  
 302  $\hat{a}_i$ . Each of the divergences can be simplified by means of Gauss's Theorem following Lee et al.  
 303 (2014).

304 (i) The computation of the mean value of the Laplacian across one hexagon of area  $\Omega = \frac{\sqrt{3}}{2} d^2$ ,  
 305 located at position  $\mathbf{p}_0$ , with neighbours at positions  $\mathbf{p}_1$ - $\mathbf{p}_6$  is

$$\begin{aligned} \langle D \nabla \cdot \nabla a_i(\mathbf{p}_0, t) \rangle &= \frac{D}{\Omega} \iint_{\Omega} \nabla \cdot \nabla a_i(\mathbf{x}, t) d\Omega = \frac{D}{\Omega} \oint \frac{\partial a_i}{\partial \hat{\mathbf{n}}} d\gamma \\ &\approx \frac{D}{\Omega} \sum_{j=1}^6 \left. \frac{\partial a_i(\mathbf{p}_j)}{\partial \hat{\mathbf{n}}} \right|_{\text{mid}} v \\ &= \frac{2D}{\sqrt{3}d^2} \sum_{j=1}^6 \frac{a_i(\mathbf{p}_j) - a_i(\mathbf{p}_0)}{d} \frac{d}{\sqrt{3}} \\ &= \frac{2D}{3d^2} \sum_{j=1}^6 (a_i(\mathbf{p}_j) - a_i(\mathbf{p}_0)), \end{aligned} \quad (7)$$

306 where  $v = d/\sqrt{3}$  is the length of each edge of the hexagon and  $d\gamma$  is an infinitesimally small distance  
 307 along its perimeter.

308 ii) The computation of the second term in Eq. 6,  $\langle a_i(\mathbf{p}_0, t) \nabla \cdot \mathbf{g}_i(\mathbf{p}_0) \rangle$ , can be written out similarly:

$$\begin{aligned} \frac{1}{\Omega} \iint_{\Omega} a_i \nabla \cdot \mathbf{g}_i d\Omega &= \frac{a_i(\mathbf{p}_0, t)}{\Omega} \oint \mathbf{g}_i \cdot d\hat{\mathbf{n}} \\ &\approx \frac{a_i(\mathbf{p}_0, t)}{\Omega} \sum_{j=1}^6 \frac{\mathbf{g}_i(\mathbf{p}_j) + \mathbf{g}_i(\mathbf{p}_0)}{2} \cdot \hat{\mathbf{n}} v \\ &= \frac{2a_i(\mathbf{p}_0, t)v}{\sqrt{3}d^2} \sum_{j=1}^6 \left[ \frac{g_i^x(\mathbf{p}_j) + g_i^x(\mathbf{p}_0)}{2} \cdot \hat{\mathbf{n}} + \frac{g_i^y(\mathbf{p}_j) + g_i^y(\mathbf{p}_0)}{2} \cdot \hat{\mathbf{n}} \right] \\ \Rightarrow \langle a_i(\mathbf{p}_0, t) \nabla \cdot \mathbf{g}(\mathbf{p}_0) \rangle &\approx \frac{a_i(\mathbf{p}_0, t)}{3d} \sum_{j=1}^6 \left[ (g_i^x(\mathbf{p}_j) + g_i^x(\mathbf{p}_0)) \cos\left(\frac{\pi}{3}(j-1)\right) + (g_i^y(\mathbf{p}_j) + g_i^y(\mathbf{p}_0)) \sin\left(\frac{\pi}{3}(j-1)\right) \right], \end{aligned} \quad (8)$$

309 where  $g_i^x$  and  $g_i^y$  are the Cartesian components of  $\mathbf{g}_i$ . Both this last expression, and the final ex-  
 310 pression of Eq. 7 can be computed locally, by summing over values of the nearest neighbours.

311 iii) The middle term in Eq. 6 is the scalar product of two vector fields which is straightforward to  
 312 compute from their Cartesian components.

313 iv) The same method used to compute  $\nabla \cdot \nabla a_i$  in term (i) is used to compute  $\nabla \cdot \nabla \hat{a}_i$ .

314 v) The final term is the scalar product of the two vector fields  $\nabla a_i$  and  $\nabla \hat{a}_i$ .

315 By separating the computation of Eq. 4 into parts (i)–(v), the no-flux boundary condition,

$$\mathbf{J}_i(\mathbf{x}, t)|_{\text{boundary}} = 0, \quad (9)$$

316 can be fulfilled. On the boundary, the contribution to  $\mathbf{J}$  resulting from the first term of Eq. 6 can be  
 317 fixed to 0 by the ‘ghost cell method’ in which, during the evaluation of (i), a hex outside the boundary  
 318 containing the same value as the hex inside the boundary is imagined to exist such that the flux of  $\mathbf{J}$   
 319 across the boundary is 0. Then,  $\mathbf{g}_i(\mathbf{x})$  can be tailored so that it, and its normal derivative, approach  
 320 0 at the boundary, ensuring that the second and third terms of Eq. 6 also contribute nothing to  $\mathbf{J}$ .  
 321 This is achieved by multiplying  $\mathbf{g}_i(\mathbf{x})$  by a sharp logistic function of the distance,  $d_b$ , from  $\mathbf{x}$  to the  
 322 boundary, of the form  $1/[1 + \exp(100(d_f - d_b))]$ , where  $d_f = 0.1 \text{ mm} \approx 3d$  is the boundary fall-off  
 323 distance.

324 The *pattern difference* metric,  $\eta$ , incorporates information about the differences in the areas of  
 325 simulated and experimentally determined (real) barrels ( $\mathcal{A}_i^{\text{sim}}$  and  $\mathcal{A}_i^{\text{exp}}$ ), as well as information  
 326 contained in the ‘adjacency vector’ for each barrel,  $\mathcal{V}_i$ , the  $j$ -th element of which is the length of  
 327 the border between barrel  $i$  and  $j$ . For a well-formed barrel pattern,  $\mathcal{V}_i$  is a sparse vector. A di-  
 328 mensionless quantity can be obtained from the scalar product of the simulated and experimental  
 329 adjacency vectors:  $\frac{1}{N} \sum_i \frac{\mathcal{V}_i^{\text{sim}}}{b_i^{\text{sim}}} \cdot \frac{\mathcal{V}_i^{\text{exp}}}{b_i^{\text{exp}}}$ , where e.g.,  $b_i^{\text{exp}}$ , is the total length of the border around real  
 330 barrel  $i$ . This quantity is small when the fields that form in simulation have dissimilar neighbour  
 331 relations to those of the real barrels (e.g., Fig. 1C,  $t = 1000$ ), and maximal for a precise topological  
 332 map ( $t = 10000$ ). A second comparison considers the mean magnitude of the difference between  
 333 the simulated and experimental vectors:  $\frac{1}{N} \sum_i \|\mathcal{V}_i^{\text{sim}} - \mathcal{V}_i^{\text{exp}}\|$ . This tends to 0 for a perfect match  
 334 and can separate patterns with straight boundaries from those with ‘noisy edges’ (as in Fig. 3B ii).

335 We combined these terms into a single metric:

$$\eta = \frac{\frac{1}{N} \sum_i \|\mathcal{A}_i^{\text{sim}} - \mathcal{A}_i^{\text{exp}}\| \times \frac{1}{N} \sum_i \|\mathcal{V}_i^{\text{sim}} - \mathcal{V}_i^{\text{exp}}\|}{\frac{1}{N} \sum_i \frac{\mathcal{V}_i^{\text{sim}}}{b_i^{\text{sim}}} \cdot \frac{\mathcal{V}_i^{\text{exp}}}{b_i^{\text{exp}}}}, \quad (10)$$

336 which has units of  $\text{mm}^3$ .

337 All code required to reproduce these results is available at <https://github.com/ABRG-Models/BarrelEmerge/tree/eLife>. The computations described in (i)–(v) may be found in the class method  
 338 RD\_James\_comp2::compute\_divJ() which calculates term1, term2, term3, term1\_1 and term1\_2, re-  
 339 spectively.

### 341 Movie S1 caption

342 Movie corresponding to Fig. 1C in the main paper. Simulation parameters were  $N = 41$ ,  $\alpha = 3.6$ ,  
 343  $\beta = 16.67$ ,  $k = 3$ ,  $D = 0.5$ ,  $\gamma \in \pm 2$ ,  $\epsilon = 1.2$  and  $\delta t = 0.0001$ . Colours indicate the thalamic projection for  
 344 which the connection density is maximal and black lines delineate boundaries. Barrel labels are  
 345 always located at the centroid of their field(s). The final frame in the movie is step 30000 of the  
 346 simulation.

### 347 Acknowledgments

348 The authors thank Jason Berwick at the University of Sheffield for advice and for access to the  
 349 rat barrel stains used to construct Fig. 1A. This work was supported by a Collaborative Activity  
 350 Award, *Cortical Plasticity Within and Across Lifetimes*, from the James S. McDonnell Foundation (grant  
 351 220020516).

## References

- 352
- 353 Agmon A, Yang LT, O'Dowd DK, Jones EG. Organized growth of thalamocortical axons from the deep tier of ter-  
354 minations into layer IV of developing mouse barrel cortex. *Journal of Neuroscience*. 1993 Dec; 13(12):5365-  
355 5382. <http://www.jneurosci.org/content/13/12/5365>, doi: 10.1523/JNEUROSCI.13-12-05365.1993.
- 356 Antón-Bolaños N, Sempere-Ferrández A, Guillamón-Vivancos T, Martini FJ, Pérez-Saiz L, Gezelius H, Filipchuk A,  
357 Valdeolmillos M, López-Bendito G. Prenatal activity from thalamic neurons governs the emergence of func-  
358 tional cortical maps in mice. *Science*. 2019 Jun; 364(6444):987-990. <https://science.science.org/content/364/6444/987>, doi: 10.1126/science.aav7617.
- 360 Armstrong-James M, Fox K, Das-Gupta A. Flow of excitation within rat barrel cortex on striking a single vib-  
361 rissa. *Journal of Neurophysiology*. 1992 Oct; 68(4):1345-1358. <https://www.physiology.org/doi/abs/10.1152/jn.1992.68.4.1345>, doi: 10.1152/jn.1992.68.4.1345.
- 363 Assimacopoulos S, Kao T, Issa NP, Grove EA. Fibroblast Growth Factor 8 Organizes the Neocortical Area Map  
364 and Regulates Sensory Map Topography. *Journal of Neuroscience*. 2012 May; 32(21):7191-7201. <http://www.jneurosci.org/content/32/21/7191>, doi: 10.1523/JNEUROSCI.0071-12.2012.
- 366 Bishop KM, Goudreau G, O'Leary DDM. Regulation of Area Identity in the Mammalian Neocortex by Emx2  
367 and Pax6. *Science*. 2000 Apr; 288(5464):344-349. <http://science.science.org/content/288/5464/344>, doi:  
368 10.1126/science.288.5464.344.
- 369 Crossley PH, Martin GR. The mouse Fgf8 gene encodes a family of polypeptides and is expressed in regions  
370 that direct outgrowth and patterning in the developing embryo. *Development*. 1995 Feb; 121(2):439-451.  
371 <https://dev.biologists.org/content/121/2/439>, publisher: The Company of Biologists Ltd Section: JOURNAL  
372 ARTICLES.
- 373 Dufour A, Seibt J, Passante L, Depaepe V, Ciossek T, Frisén J, Kullander K, Flanagan JG, Polleux F, Vanderhaeghen  
374 P. Area Specificity and Topography of Thalamocortical Projections Are Controlled by ephrin/Eph Genes.  
375 *Neuron*. 2003 Jul; 39(3):453-465. <http://www.sciencedirect.com/science/article/pii/S0896627303004409>, doi:  
376 10.1016/S0896-6273(03)00440-9.
- 377 Erzurumlu RS, Gaspar P. Development and critical period plasticity of the barrel cortex: Barrel cortex plasticity.  
378 European Journal of Neuroscience. 2012 May; 35(10):1540-1553. <http://doi.wiley.com/10.1111/j.1460-9568.2012.08075.x>, doi: 10.1111/j.1460-9568.2012.08075.x.
- 380 Gao PP, Yue Y, Zhang JH, Cerretti DP, Levitt P, Zhou R. Regulation of thalamic neurite outgrowth by the  
381 Eph ligand ephrin-A5: Implications in the development of thalamocortical projections. *Proceedings of the  
382 National Academy of Sciences*. 1998 Apr; 95(9):5329-5334. <https://www.pnas.org/content/95/9/5329>, doi:  
383 10.1073/pnas.95.9.5329, publisher: National Academy of Sciences Section: Biological Sciences.
- 384 Haidarliu S, Ahissar E. Size gradients of barreloids in the rat thalamus. *Journal of Comparative Neurology*.  
385 2001; 429(3):372-387. <https://onlinelibrary.wiley.com/doi/abs/10.1002/1096-9861%2820010115%29429%3A3%3C372%3A%3AAID-CNE2%3E3.0.CO%3B2-3>, doi: 10.1002/1096-9861(20010115)429:3<372::AID-CNE2>3.0.CO;2-3.
- 388 Honda H. Geometrical Models for Cells in Tissues. In: *International Review of Cytology*, vol. 81 Else-  
389 vier; 1983.p. 191-248. <https://linkinghub.elsevier.com/retrieve/pii/S0074769608623396>, doi: 10.1016/S0074-  
390 7696(08)62339-6.
- 391 Jeanmonod D, Rice FL, Van der Loos H. Mouse somatosensory cortex: Alterations in the barrelfield fol-  
392 lowing receptor injury at different early postnatal ages. *Neuroscience*. 1981 Aug; 6(8):1503-1535. <http://www.sciencedirect.com/science/article/pii/0306452281902220>, doi: 10.1016/0306-4522(81)90222-0.
- 394 Karbowski J, Ermentrout GB. Model of the Early Development of Thalamo-Cortical Connections and Area  
395 Patterning via Signaling Molecules. *Journal of Computational Neuroscience*. 2004 Nov; 17(3):347-363. <http://link.springer.com/10.1023/B:J CNS.0000044876.28268.18>, doi: 10.1023/B:J CNS.0000044876.28268.18.
- 397 Kossut M. Effects of sensory deprivation upon a single cortical vibrissal column: a 2DG study. *Experimental  
398 brain research*. 1992; 90(3):639-642. Publisher: Springer.
- 399 Land PW, Simons DJ. Metabolic activity in Sml cortical barrels of adult rats is dependent on patterned sensory  
400 stimulation of the mystacial vibrissae. *Brain Research*. 1985 Aug; 341(1):189-194. <http://www.sciencedirect.com/science/article/pii/000689938591488X>, doi: 10.1016/0006-8993(85)91488-X.

- 402 Lee D, Tien HC, Luo CP, Luk HN. Hexagonal grid methods with applications to partial differential equations.  
 403 International Journal of Computer Mathematics. 2014 Sep; 91(9):1986–2009. <http://www.tandfonline.com/doi/abs/10.1080/00207160.2013.864392>, doi: 10.1080/00207160.2013.864392.
- 405 Ma PM. The barrelettes—architectonic vibrissal representations in the brainstem trigeminal complex of the  
 406 mouse. Normal structural organization. Journal of Comparative Neurology. 1991; 309(2):161–199. <https://onlinelibrary.wiley.com/doi/abs/10.1002/cne.903090202>, doi: 10.1002/cne.903090202.
- 408 Miller K, Kolk SM, Donoghue MJ. EphA7-ephrin-A5 signaling in mouse somatosensory cortex: Develop-  
 409 mental restriction of molecular domains and postnatal maintenance of functional compartments. The  
 410 Journal of Comparative Neurology. 2006 Jun; 496(5):627–642. <http://doi.wiley.com/10.1002/cne.20926>, doi:  
 411 10.1002/cne.20926.
- 412 Purves D, Riddle DR, LaMantia AS. Iterated patterns of brain circuitry (or how the cortex gets its spots). Trends  
 413 in Neurosciences. 1992 Jan; 15(10):362–368. <https://linkinghub.elsevier.com/retrieve/pii/016622369290180G>,  
 414 doi: 10.1016/0166-2236(92)90180-G.
- 415 Sehara K, Kawasaki H. Neuronal Circuits with Whisker-Related Patterns. Molecular Neurobiology. 2011 Jun;  
 416 43(3):155–162. <https://doi.org/10.1007/s12035-011-8170-8>, doi: 10.1007/s12035-011-8170-8.
- 417 Senft SL, Woolsey TA. Mouse Barrel Cortex Viewed as Dirichlet Domains. Cerebral Cortex. 1991; 1(4):348–363.  
 418 <https://academic.oup.com/cercor/article-lookup/doi/10.1093/cercor/1.4.348>, doi: 10.1093/cercor/1.4.348.
- 419 Shimogori T, Grove EA. Fibroblast Growth Factor 8 Regulates Neocortical Guidance of Area-Specific Thalamic  
 420 Innervation. Journal of Neuroscience. 2005 Jul; 25(28):6550–6560. <http://www.jneurosci.org/content/25/28/6550>, doi: 10.1523/JNEUROSCI.0453-05.2005.
- 422 Speer CM, Chapman B. Grading the thalamus: how can an ‘Eph’ be excellent? Thalamus and Re-  
 423 lated Systems. 2005 Sep; 3(03):235. [http://www.journals.cambridge.org/abstract\\_S1472928807000234](http://www.journals.cambridge.org/abstract_S1472928807000234), doi:  
 424 10.1017/S1472928807000234.
- 425 Sperry RW. Chemoaffinity in the Orderly Growth of Nerve Fiber Patterns and Connections. Proceedings of  
 426 the National Academy of Sciences. 1963 Oct; 50(4):703–710. <https://www.pnas.org/content/50/4/703>, doi:  
 427 10.1073/pnas.50.4.703.
- 428 Torii M, Rakic P, Levitt P. Role of EphA/ephrin-A signaling in the development of topographic  
 429 maps in mouse corticothalamic projections. Journal of Comparative Neurology. 2013; 521(3):626–  
 430 637. <https://onlinelibrary.wiley.com/doi/abs/10.1002/cne.23195>, doi: 10.1002/cne.23195, \_eprint:  
 431 <https://onlinelibrary.wiley.com/doi/pdf/10.1002/cne.23195>.
- 432 Van Der Loos H. Barreloids in mouse somatosensory thalamus. Neuroscience Letters. 1976 Mar; 2(1):1–6.  
 433 <http://www.sciencedirect.com/science/article/pii/0304394076900367>, doi: 10.1016/0304-3940(76)90036-7.
- 434 Vanderhaeghen P, Lu Q, Prakash N, Frisén J, Walsh CA, Frostig RD, Flanagan JG. A mapping label required  
 435 for normal scale of body representation in the cortex. Nature Neuroscience. 2000 Apr; 3(4):358–365. [https://www.nature.com/articles/nn0400\\_358](https://www.nature.com/articles/nn0400_358), doi: 10.1038/73929.
- 437 Vanderhaeghen P, Polleux F. Developmental mechanisms patterning thalamocortical projections: intrinsic,  
 438 extrinsic and in between. Trends in Neurosciences. 2004 Jul; 27(7):384–391. <http://www.sciencedirect.com/science/article/pii/S0166223604001638>, doi: 10.1016/j.tins.2004.05.009.
- 440 Woolsey TA, Van der Loos H. The structural organization of layer IV in the somatosensory region (S I) of  
 441 mouse cerebral cortex: The description of a cortical field composed of discrete cytoarchitectonic units. Brain  
 442 Research. 1970 Jan; 17(2):205–242. <http://www.sciencedirect.com/science/article/pii/000689937090079X>, doi:  
 443 10.1016/0006-8993(70)90079-X.
- 444 Woolsey TA, Welker C, Schwartz RH. Comparative anatomical studies of the Sml face cortex with special refer-  
 445 ence to the occurrence of “barrels” in layer IV. The Journal of Comparative Neurology. 1975 Nov; 164(1):79–94.  
 446 <http://doi.wiley.com/10.1002/cne.901640107>, doi: 10.1002/cne.901640107.
- 447 Zheng Y, Johnston D, Berwick J, Mayhew J. Signal Source Separation in the Analysis of Neural Activity in Brain.  
 448 Neurolimage. 2001 Mar; 13(3):447–458. <https://linkinghub.elsevier.com/retrieve/pii/S1053811900907055>, doi:  
 449 10.1006/nimg.2000.0705.